analytical chemistry

pubs.acs.org/ac Article

Hollow Double-Shell $CuCo_2O_4$@Cu_2O Heterostructures as a Highly Efficient Coreaction Accelerator for Amplifying NIR Electrochemiluminescence of Gold Nanoclusters in Immunoassay

Hongying Jia,† Jingshuai Li,† Lei Yang, Dawei Fan, Xuan Kuang, Xu Sun, Qin Wei,* and Huangxian Ju

Cite This: *Anal. Chem.* 2022, 94, 7132−7139 Read Online

ACCESS | Metrics & More | Article Recommendations | Supporting Information

ABSTRACT: The evolution of electrochemiluminescence (ECL) emission amplified by coreaction accelerator in near-infrared (NIR) area has been overwhelmingly anticipated for ultrasensitive detection of disease biomarkers. Herein, the hollow double-shell $CuCo_2O_4$@Cu_2O (HDS-$CuCo_2O_4$@Cu_2O) heterostructures were conveniently prepared and utilized as an attractive coreaction accelerator to improve the NIR ECL performance of gold nanoclusters (AuNCs) for the first time. Benefiting from perfect-matched lattice spacing, unique Cu_2O nanoparticles (NPs) were formed in situ on the layered-hollow $CuCo_2O_4$ nanospheres (NSs) to obtain HDS-$CuCo_2O_4$@Cu_2O heterostructures. The formed heterojunctions supplied shorter charge transfer distance and better interfacial charge transfer efficiency as well as more effective separation performance. Consequently, HDS-$CuCo_2O_4$@Cu_2O heterostructures as an admirable electroactive substrate could significantly promote the formation of sufficient coreactant intermediate radicals to react with AuNCs cationic radicals, realizing about 3-folds stronger NIR ECL response than that of individual AuNCs. In addition, the AuNCs templated by L-methionine (L-Met) exhibited NIR ECL emission around 830 nm, which could decrease the photochemical damage to even realize a nondestructive detection with improved susceptibility and circumambient adaptability. Subsequently, a well site-oriented fixation strategy utilizing HWRGWVC heptapeptide as the specific antibody immobilizer was introduced to further preserve the bioactivity of antibody on the HDS-$CuCo_2O_4$@Cu_2O and AuNCs surface along with enhancing the incubation performance markedly. In view of the progressive sensing mechanism, a NIR immunosensor was obtained for the ultrasensitive analysis of CYFRA21−1, which achieved a broad linear ranging from 2 fg/mL to 50 ng/mL and a low limit of detection (LOD) of 0.67 fg/mL (S/N = 3).

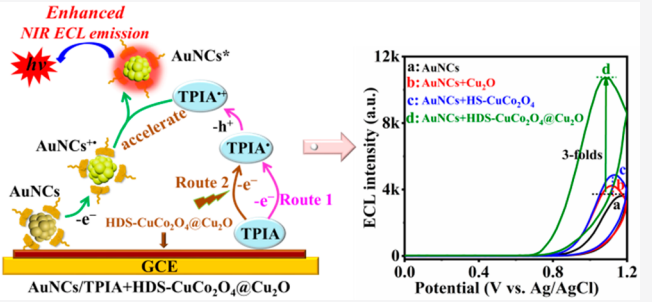

Electrochemiluminescence (ECL) involves the electrochemically triggered energy-relaxation phenomenon in which the luminophore can utilize electron-transfer to achieve excited states for emitting light.[1−4] ECL has been extensively identified to be a persuasive analytical technique with merits of intrinsically low background, high sensitivity, broad detection range, and admirable controllability.[5,6] Recently, Au nanoclusters (AuNCs) as one of the most burgeoning electrochemiluminophores have obtained remarkable attention owing to their distinctive chemical, electrical, and optical characteristics.[7−11] In particular, L-methionine (L-Met) stabilized AuNCs with admirable biocompatibility not only act as a near-infrared (NIR) signal label with improved susceptibility and circumambient adaptability,[12] but also function as a linker for the decoration of immunizing molecules via sufficient functional groups supplied by L-Met.[13,14] However, AuNCs usually undergo poor ECL efficiency due to the depressed charges transfer efficiency in the electrogenerated procedure and plentiful nonradiative transition of excited species in the energy relaxed process.[15−17] More recently, the biocompatible AuNCs with property of aggregation induced emission (AIE) have been exploited to promote the ECL efficiency via inhibiting the nonradiative transition.[18,19] However, the insufficient charge-transfer mechanism during electrochemical redox of AuNCs has not been systematically solved and still results in the inferior NIR ECL efficiency, which becomes primary factor that affects the widespread application and sensitive bioassay. Then, it is anticipated to implement considerable endeavors to explore appropriately supplementary methods for enhancing the charge transfer and facilitating the NIR ECL efficiency of AuNCs.

Fortunately, the enhanced ECL emission through coreactant acceleration have been achieved by promoting the electron transfer to form more electroactive radicals for generating photons.[20,21] Amazingly, some nanomaterials have consider-

Received: March 15, 2022
Accepted: April 26, 2022
Published: May 6, 2022

https://doi.org/10.1021/acs.analchem.2c01162
Anal. Chem. 2022, 94, 7132−7139

Scheme 1. Preparation of (A) AuNCs-HWR-Ab_2 Bioconjugates and (B) HDS-$CuCo_2O_4$@Cu_2O-HWR; (C) Fabrication Procedure of the NIR Immunosensor

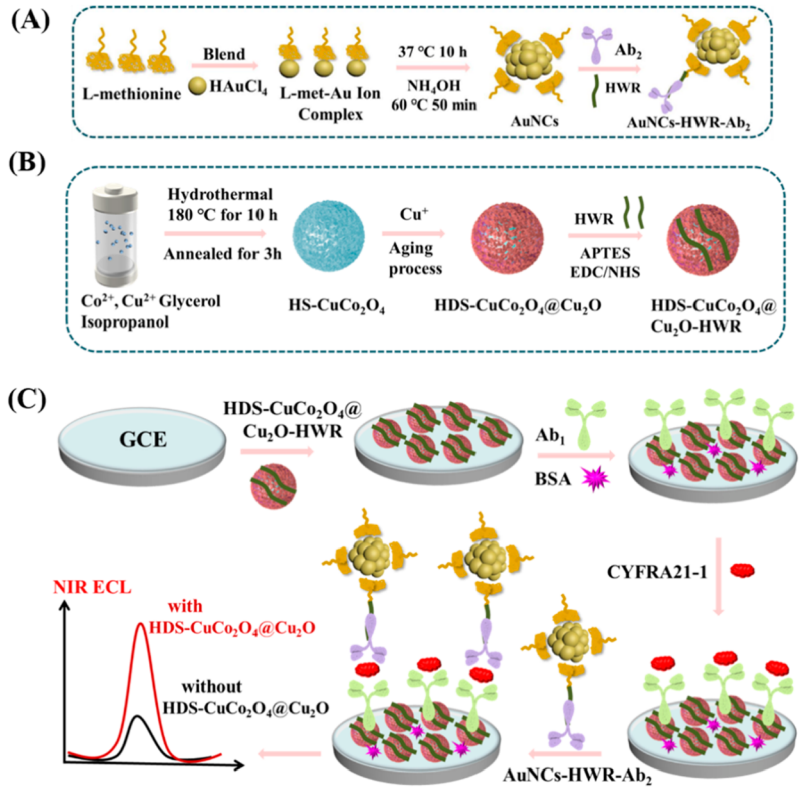

ably enhanced the ECL emission of AuNCs through the coreaction accelerated route. For instance, Yuan's group utilized TiO_2 nanosheets (NSs) to disintegrate coreactant H_2O_2 and promoted the ECL response of Au_{25}NCs successfully.[22] Meanwhile, they also employed Pd@CuO to promote the ECL performance of AuNCs with tris(3-aminoethyl)amine (TAEA) as the coreactant via immobilizing them into one nanostructure.[5] Moreover, the exploration about Cu_2O and Cu_2S as the coreaction accelerator have been achieved by our groups, which was owing to the perfect redox reversibility of Cu^+/Cu^{2+}.[23,24] However, investigation on heterostructures as the coreactant triisopropanolamine (TPIA) accelerator for improving the NIR ECL efficiency of AuNCs is still in its infancy. Inspired by this, n-type $CuCo_2O_4$ hollow spheres (HS-$CuCo_2O_4$) with merits of large specific surface area and efficient charge separation efficiency in the interior cavity were selected as favorable substrate to support the representative p-type semiconductor of Cu_2O to fabricate the hollow double-shell $CuCo_2O_4$@Cu_2O (HDS-$CuCo_2O_4$@Cu_2O) heterostructures.[25] The formed heterojunctions supplied shorter charge transfer distance and possessed better interfacial charge transfer efficiency with more effective separation efficiency, which displayed excellent capacity for promoting the generation of electroactive radicals of coreactant to amplify ECL signal.[26]

Benefiting from aforementioned discussion, we have first prepared an ECL immunosensor with AuNCs as the luminophore and HDS-$CuCo_2O_4$@Cu_2O heterostructures as the coreactant accelerator for the sensitive detection of CYFRA21−1. CYFRA21−1, the soluble segment of cytokeratin 19, presents in cytoplasm of tumor cells and becomes the most sensitive biomarker for the diagnosis and prognostic of nonsmall cell lung cancer (NSCLC).[27] The level of CYFRA 21−1 is associated with the process of disease. According to the immunosensor, amine-functionalized HDS-$CuCo_2O_4$@Cu_2O was regarded as the electroactive substrate to modify the capture antibody (Ab_1) for fabricating sensing platform, and L-Met was selected as the surface stabilizer to synthesize AuNCs for connecting Ab_2 with the ECL emission at NIR 830 nm. The NIR ECL emission could obviously decrease the photochemical damage to test samples and even achieved a nondestructive detection with low background. In addition, to preserve the biological activity of antibodies, HWRGWVC (HWR), a heptapeptide with the advantages of specifically recognizing the Fc portion in the antibody by a site-oriented strategy and enhancing incubating performance, was introduced to the surface of HDS-$CuCo_2O_4$@Cu_2O and AuNCs via the amine reaction.[26,28] Based on the above superiorities, the proposed NIR ECL immunosensor displayed an admirable linearity ranging from 2 fg/mL to 50 ng/mL with the low limit of detection (LOD) of 0.67 fg/mL.

EXPERIMENTAL SECTION

Fabrication of Proposed NIR ECL Immunosensor. The chemicals and materials, apparatus, and preparation of HDS-$CuCo_2O_4$@Cu_2O-HWR and AuNCs-HWR-Ab_2 bioconjugates are displayed in the Supporting Information (SI). The fabricated process of the NIR ECL immunosensor was illustrated in Scheme 1. Bare glassy carbon electrode (GCE) was burnished by Al_2O_3 slurries, washed with ultrapure water, and dried under N_2 atmosphere for the subsequent modification. First, HDS-$CuCo_2O_4$@Cu_2O-HWR (10 μL, 2 mg/mL) was decorated on GCE surface and rinsed with phosphate buffered saline (PBS, 0.1 mol/L, pH 7.4). Second,

https://doi.org/10.1021/acs.analchem.2c01162
Anal. Chem. 2022, 94, 7132−7139

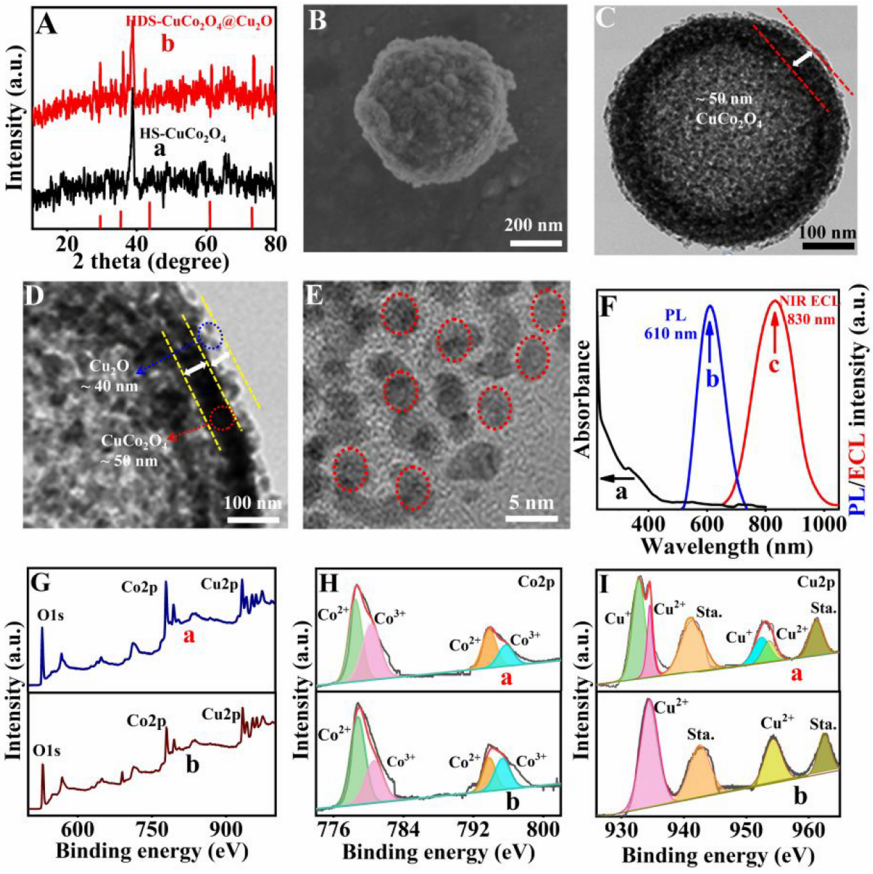

Figure 1. (A) XRD patterns for HS-$CuCo_2O_4$ (a) and HDS-$CuCo_2O_4$@Cu_2O (b), (B) SEM image of HS-$CuCo_2O_4$, HRTEM images of (C) HS-$CuCo_2O_4$, (D) HDS-$CuCo_2O_4$@Cu_2O and (E) AuNCs, (F) UV−vis absorption (a), PL (b) and ECL spectra (c) of AuNCs, (G) XPS survey spectra of HDS-$CuCo_2O_4$@Cu_2O (a) and HS-$CuCo_2O_4$ (b), and the high resolution spectra of Co 2p (H) and Cu 2p (I) for HDS-$CuCo_2O_4$@Cu_2O (a) and HS-$CuCo_2O_4$ (b).

the as-prepared Ab_1 solution (10 μL, 10 μg/mL) was coated on the HDS-$CuCo_2O_4$@Cu_2O-HWR surface and the incubated process was achieved at 4 °C for 60 min. After sealing the nonspecific active sites with bovine serum albumin (BSA) (3 μL, 0.1 wt %), 10 μL of various contents of CYFRA21−1 were dropped on the electrode surface for incubating 60 min at 37 °C. Lastly, AuNCs-HWR-Ab_2 (10 μL) bioconjugate as the signal label was connected with CYFRA21−1 to accomplish the immunosensor modification.

Electrochemical and ECL Measurements. Cyclic voltammetry (CV) and ECL were applied for the analysis, respectively. The relevant ECL performance was achieved in 10 mL of PBS (0.1 mol/L, pH 7.4) containing 0.1 mol/L TPIA as the coreactant with parameters as follows: photomultiplier tube voltage (800 V), scanning voltage (0−1.2 V), and scanning rate (0.15 V/s).

RESULTS AND DISCUSSION

Characterizations of HS-$CuCo_2O_4$, HDS-$CuCo_2O_4$@Cu_2O and Luminous AuNCs Nanostructure. The detailed crystallographic construction of the nanostructures were demonstrated by X-ray diffraction (XRD). All the peaks in the XRD pattern of HS-$CuCo_2O_4$ were accorded with the standard pattern of JCPDS No. 71−0816 (Figure 1A, curve a). The characteristic peaks of Cu_2O nanoparticles were at 2θ degree of 29.6°, 36.5°, 42.3°, 61.4°, and 73.6°, which could match with (1 1 0), (1 1 1), (2 0 0), (2 2 0), and (1 1 0) of cubic Cu_2O (JCPDS No. 05−0667). Then, after the acquisition of HDS-$CuCo_2O_4$@Cu_2O nanostructure (Figure 1A curve b), except the relevant HS-$CuCo_2O_4$ peaks, the diffraction peaks of Cu_2O were also exhibited, which indicated the formation of HDS-$CuCo_2O_4$@Cu_2O. The Figure 1B exhibited the scanning electron microscope (SEM) image of HS-$CuCo_2O_4$, the as-prepared HS-$CuCo_2O_4$ possessed an obvious sphere-like nanostructure with the rough surface and average diameter around 500 nm. Subsequently, the hollow nanostructure of $CuCo_2O_4$ was proved by high resolution transmission electron microscopy (HRTEM) image of Figure 1C, and the average thickness of $CuCo_2O_4$ shell was approximate 50 nm. After the covering of Cu_2O, the $CuCo_2O_4$@Cu_2O demonstrated the enhanced average size of 600 nm (Figure 1D), and also exhibited the thickness of 50 nm for $CuCo_2O_4$ and 40 nm for Cu_2O, respectively, which further verified its hollow double-shell nanostructure. Furthermore, the HRTEM (Figure 1D) analysis of hollow $CuCo_2O_4$ and layer Cu_2O revealed the suitable contact facets between them, which could be contributed to the formation of HDS-$CuCo_2O_4$@Cu_2O heterojuctions.

Notably, with the purpose of investigating the morphology and size of as-prepared luminous AuNCs, the HRTEM image (Figure 1E) and size-distribution histogram pattern (Supporting Information (SI) Figure S1) were exhibited. It can be seen that AuNCs exhibited uniform particle diameter of 2.8 ± 0.5 nm with monodisperse distribution. According to Figure 1F,

https://doi.org/10.1021/acs.analchem.2c01162
Anal. Chem. 2022, 94, 7132−7139

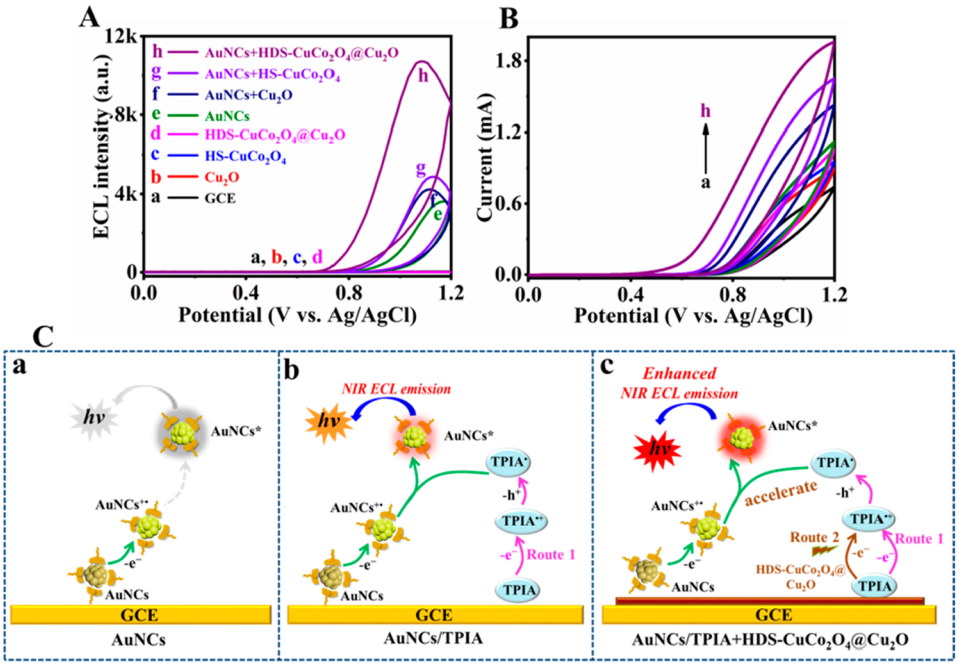

Figure 2. (A) ECL-potential profiles and (B) CV curves for AuNCs/TPIA, and (C) mechanistic illustrations of AuNCs without coreactant (a), AuNCs/TPIA system (b), and AuNCs/TPIA system with HDS-$CuCo_2O_4$@Cu_2O as coreaction accelerator (c).

AuNCs displayed a remarkable reduce in the absorbance spectrum with the enhanced wavelength inside the ultraviolet region and it displayed a broad shoulder with a tail inside the visible range (Figure 1F, curve a). Meanwhile, they were without the surface plasmon resonance peak of Au nanoparticles (AuNPs) around 520 nm, indicating the small dimension of as-prepared AuNCs. Photoluminescence (PL) spectrum of AuNCs displayed a broad peak along with maximum wavelength at 610 nm (Figure 1F, curve b). In addition, the maximum NIR ECL emission wavelength (Figure 1F, curve c) of AuNCs was around 830 nm, which was red-shifted for 220 nm in regard to its PL spectrum. The 220 nm red-shift might be owing to the different exciation manners among the ECL and PL in AuNCs, whereas the PL was obtained via the exciation and emission inside the core, and the ECL was attributed to the surface state.[29,30]

The chemical compositions and elemental valence states of HS-$CuCo_2O_4$ and HDS-$CuCo_2O_4$@Cu_2O were assessed by X-ray photoelectron spectroscopy (XPS) as displayd in Figure 1G–I. The survey spectra in Figure 1G demonstrated the existence of Co, Cu, and O. Meanwhile, the high resolution spectra of Co 2p, Cu 2p for HS-$CuCo_2O_4$ and HDS-$CuCo_2O_4$@Cu_2O were exhibited in Figure 1H,I. Upon the high resolution spectrum of Co 2p (Figure 1H), the two distinct peaks centered at 779.6 and 794.6 eV were assigned to Co^{2+}, while another two peaks located at 781.0 and 796.0 eV belonged to Co^{3+}, demonstrating the coexistence for Co^{2+} and Co^{3+} in the HS-$CuCo_2O_4$ and HDS-$CuCo_2O_4$@Cu_2O.[31] Interestingly, in the Cu 2p region (Figure 1I), the peaks appeared at 934.7 and 954.7 eV along with the typical satellite peaks belonging to the Cu $2p_{3/2}$ and Cu $2p_{1/2}$ for Cu^{2+} in HS-$CuCo_2O_4$.[32] After covering the HS-$CuCo_2O_4$ by Cu_2O layer, the Cu 2p spectrum was divided into four obvious peaks located at 932.8, 934.7, 952.7, and 954.7 eV, belonging to Cu^+ ($2p_{3/2}$), Cu^{2+} ($2p_{3/2}$), Cu^+ ($2p_{1/2}$), and Cu^{2+} ($2p_{1/2}$), respectively.[33] Besides, the relevant O 1s spectrum was divided into two peaks around 530.0 and 531.6 eV (SI Figure 2S), which could be attributed to metal (Cu, Co) with oxygen bonds (i.e., M–O) and –OH structure.[34]

Enhancement of ECL Performance by HDS-$CuCo_2O_4$@Cu_2O Heterostructures. The significant role of HDS-$CuCo_2O_4$@Cu_2O heterostructures in the AuNCs-TPIA system was investigated. As exhibited in Figure 2A,B, the explorations about synchronous ECL and CV under diffferent conditions were illustrated. No ECL response was acquired from the GCE (Figure 2A, curve a). After the modification onto GCE with Cu_2O (2 mg/mL), HS-$CuCo_2O_4$ (2 mg/mL) and HDS-$CuCo_2O_4$@Cu_2O (2 mg/mL) in PBS (pH 7.4) including 0.1 mol/L TPIA (Figure 2A, curves b–d), no ECL emissions were displayed. When the AuNCs (100 μg/mL), AuNCs with Cu_2O (AuNCs+Cu_2O) and HS-$CuCo_2O_4$ (AuNCs+HS-$CuCo_2O_4$) with the same concentration were dropped on the GCE, obvious ECL signals with intensities of 3609 au, 4222 au, and 4896 au could be obtained in PBS (pH 7.4) including 0.1 mol/L TPIA (Figure 2A, curves e–g), which verified that the ECL emission of AuNCs was increased by Cu_2O and HS-$CuCo_2O_4$. However, after modifying the GCE by the AuNCs with HDS-$CuCo_2O_4$@Cu_2O (AuNCs+HDS-$CuCo_2O_4$@Cu_2O) under uniform condition (Figure 2A, curve h), it exhibited a significant ECL response (10787 au) and the enhanced response by HDS-$CuCo_2O_4$@Cu_2O was obviously higher than the individual Cu_2O and HS-$CuCo_2O_4$. Moreover, the ECL emission potentials became more and more positive (Figure 2A, curves e–h), and the AuNCs with HDS-$CuCo_2O_4$@Cu_2O displayed the lowest triggered potential of 1.05 V. Furthermore, corresponding CV measurements were exhibited in Figure 2B. The GCE/AuNCs+HDS-$CuCo_2O_4$@Cu_2O showed the strongest current and the lowest onset potential, which demonstrated that HDS-$CuCo_2O_4$@Cu_2O played a crucial role of promoting the electron transfer.

Possible ECL Mechanism for Signal Amplification. On account of above experimental consequences, the probable

https://doi.org/10.1021/acs.analchem.2c01162
Anal. Chem. 2022, 94, 7132–7139

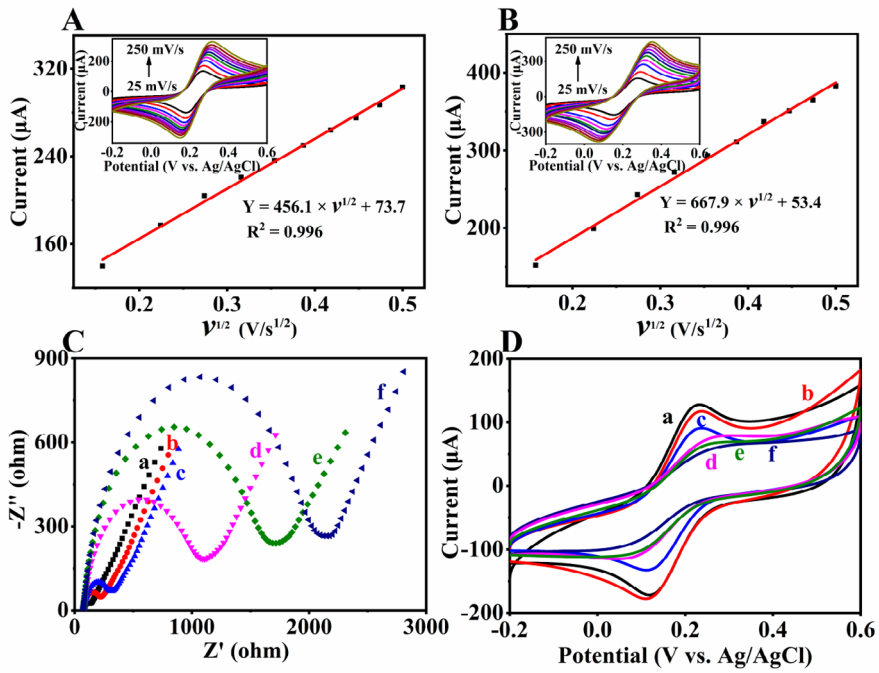

Figure 3. CV curves and linear relations of electrodes modified with (A) HS-$CuCo_2O_4$ and (B) HDS-$CuCo_2O_4$@Cu_2O in 5.0 mmol/L $Fe(CN)_6^{3-/4-}$ with the scan rate range of 25−250 mV/s, (C) EIS and (D) CV profiles of stepwise-modified electrodes in 0.1 mol/L PBS containing 5 mmol/L $Fe(CN)_6^{3-/4-}$: (a) GCE, (b) HDS-$CuCo_2O_4$@Cu_2O-HWR/GCE, (c) Ab_1/HDS-$CuCo_2O_4$@Cu_2O-HWR/GCE, (d) BSA/Ab_1/HDS-$CuCo_2O_4$@Cu_2O-HWR/GCE, (e) CYFRA21−1/BSA/Ab_1/HDS-$CuCo_2O_4$@Cu_2O-HWR/GCE, (f) AuNCs-HWR-Ab_2/CYFRA21−1/BSA/Ab_1/HDS-$CuCo_2O_4$@Cu_2O-HWR/GCE.

ECL mechanism of the proposed NIR ECL immunosensor was displayed in Figure 2C. Owing to the absence of coreactant (SI Figure S3), no effective ECL response of AuNCs could be obtained (a). When TPIA was utilized as the coreactant, $TPIA^{\bullet+}$ was generated around the surface of GCE, which resulted in a good ECL emission (b). Notably, as HDS-$CuCo_2O_4$@Cu_2O participated into the ECL generative procedure (c), the formation of $TPIA^{\bullet+}$ was obviously enhanced, which obtained outstanding ECL signal enlargement. Then, a probable mechanism of the NIR ECL immunosensor was exhibited as follows (eqs 1-5). In addition, the enhanced ECL mechanism for AuNCs and HDS-$CuCo_2O_4$@Cu_2O was probably through the heterojunctions between Cu_2O and HS-$CuCo_2O_4$ as displayed in SI Figure S4. Cu_2O and HS-$CuCo_2O_4$ were considered as p-type and n-type semiconductors, respectively.

Among the heterojunctions of tight solid−solid interfacial contact between them, the generated e^-/h^+ pairs in the heterojunctions interface supplied shorter charge transfer distance, better interfacial charge transfer efficiency and more effective separation efficiency.[25] Thus, the hole of HDS-$CuCo_2O_4$@Cu_2O obtained electron from TPIA to promote the formation of $TPIA^{\bullet+}$, which led to more $TPIA^{\bullet}$ in unit time via the deprotonation procedure.[35] As shown in SI Figure S5, the electron paramagnetic resonance (EPR) spectra also demonstrated that the heterojunctions could efficiently promote the generation of $TPIA^{\bullet+}$. Besides, the HS-$CuCo_2O_4$ and Cu_2O could accelerate the formation of $TPIA^{\bullet+}$ by the catalytic performance with the convertible valence of Cu^+/Cu^{2+} and Co^{2+}/Co^{3+}.[12] While the AuNCs underwent a oxidative reaction to form positively charged Au radical ($Au^{+\bullet}$), $TPIA^{\bullet}$ offered one electron for transferring it to $Au^{+\bullet}$ along with forming Au* (eq 4) to emit ECL,[18,36] meanwhile, more $TPIA^{\bullet}$ generated by HDS-$CuCo_2O_4$@Cu_2O woud enhance the ECL response. That is, the synergetic effect between TPIA oxidation and h^+ generation from the HDS-$CuCo_2O_4$@Cu_2O heterostructures accelerates the production of $TPIA^{\bullet+}$, which endows the HDS-$CuCo_2O_4$@Cu_2O heterostructures present a great promotion for TPIA oxidation. The enhanced NIR ECL emission was below.

■ ENHANCED NIR ECL EMISSION

$$AuNCs - e^- \rightarrow Au\,NCs^{+\bullet} \quad (1)$$

$$TPIA + h^+ \rightarrow (HDS - CuCo_2O_4@Cu_2O)TPIA^{\bullet+}(\textbf{more}) \quad (2)$$

$$TPTA^{\bullet+} \rightarrow TPIA^{\bullet} + H^+ \quad (3)$$

$$Au\,NCs^{+\bullet} + TPIA^{\bullet} \rightarrow AuNCs^* \quad (4)$$

$$AuNCs^* \rightarrow AuNCs + h\nu(830nm) \quad (5)$$

Enhanced Electroactive Surface Area of HDS-$CuCo_2O_4$@Cu_2O Heterostructures. The electrochemical characteristic of HS-$CuCo_2O_4$ would be obviously increased by the coating layer of Cu_2O, which could be substantiated through the enhancement of electroactive surface range. In order to implement the exploration, GCEs were decorated by HS-$CuCo_2O_4$ and HDS-$CuCo_2O_4$@Cu_2O heterostructures, respectively. All CV curves were obtained by applying the conventional $Fe(CN)_6^{3-/4-}$ as the redox couple. The linear equations are $Y = 456.1 \times \nu^{1/2} + 73.7$ and $Y = 667.9 \times \nu^{1/2} + 53.4$, respectively. On the basis of Randles−Sevcik equation[37,38]

$$I_p = (2.69 \times 10^5)AD^{1/2}n^{3/2}\nu^{1/2}c$$

https://doi.org/10.1021/acs.analchem.2c01162
Anal. Chem. 2022, 94, 7132−7139

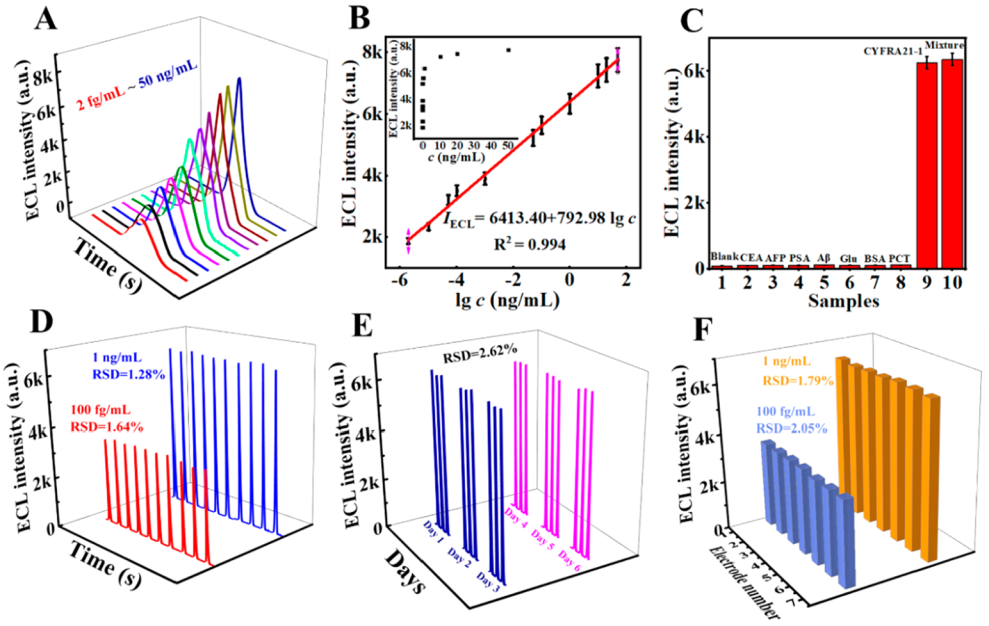

Figure 4. (A) ECL intensity-time curves, (B) corresponding calibration curve of the immunosensor for different concentrations of CYFRA21−1 (2 fg/mL to 50 ng/mL) in 0.1 mol/L PBS (pH 7.4) with 0.1 mol/L TPIA, (C) selectivity of the prepared immunosensor to different targets, (D) operational stability of the prepared immunosensor under continuous potential scanning for 10 circles, (E) positioned stability of the obtained immunosensor and (F) reproducibility of the immunosensor with the detection of seven different electrodes. Inset of 4B: the relationship between the ECL intensity and concentration of CYFRA21−1.

It could be marked that *Ip* represents the peak reductive current of $K_3Fe(CN)_6$, A represents the electroactive range (cm^2) of electrodes decorated by various nanomaterials, n represents the quantity of conveyed electrons among the redox (n = 1), c means the content of corresponding $K_3Fe(CN)_6$ (c = 5 mmol/L), D means the diffused coefficient of $Fe(CN)_6^{3-/4-}$ (D = 6.70 × 10^{-6} cm^2/s at 25 °C), then the v means the CV sweeping rate (V/s). On account of Randles−Sevcik equation, A results of HS-$CuCo_2O_4$ decorated GCE (Figure 3A) and HDS-$CuCo_2O_4$@Cu_2O (Figure 3B) decorated GCE were 18.5 and 26.2 mm^2, which demonstrated that HDS-$CuCo_2O_4$@Cu_2O heterostructures with the electroactive range and electron transfer rate were more conductive for catalysis.

Feasibility of NIR ECL Immunosensing. The electrochemical impedance spectroscopy (EIS) and CV were applied to estimate the assembled process of the NIR immunosensor as displayed in Figure 3C,D.

The EIS of GCE displayed a little semicircle (Figure 3C, curve a), which was because of free electron transfer. After dropping HDS-$CuCo_2O_4$@Cu_2O-HWR onto surface of GCE, the semicircle enhanced owing to hindrance of electron transfer (Figure 3C, curve b). Subsequently, with continuous decoration of Ab_1, BSA and CYFRA21−1 onto GCE, the resistance increased step by step (Figure 3C, curves c−e). Next then, the resistance further enhanced by the eventual modification of AuNCs-HWR-Ab_2 bioconjugates (Figure 3C, curve f), demonstrating the excellent construction of the immunosensor. Furthermore, CV was also an effective and facile electrochemical strategy for monitoring the installed process of the NIR ECL immunosensor (Figure 3D). The smaller and smaller peak current with promoted peak potential separation could been shown after the continuous modification of GCE, which indicated the obstruction for electron transfer and the successful decoration of prepared immunosensor.

Performance of the NIR ECL Immunosensing for CYFRA21−1 Detection. After optimizing the experimental conditions (SI Figure S6), the property of the proposed NIR immunosensor was studied by incubating various contents of CYFRA21−1. As exhibited in Figure 4A, the ECL response promoted successively when the contents of CYFRA21−1 enhanced from 2 fg/mL to 50 ng/mL. Besides, the obtained ECL signals showed a perfect linear relation with the logarithm of CYFRA21−1 content as exhibited in Figure 4B. The corresponding linear regression equation was I = 6413.40 + 792.98 lg c (R^2 = 0.994). The obtained LOD was 0.67 fg/mL (S/N = 3), which possessed higher sensitivity than those of previous reports (SI Table S1). As a consequence, the obtained immunosensor achieved an ultrasensitive detection for CYFRA21−1.

Selectivity, Stability, and Reproducibility of the NIR Biosensor. Selectivity, stability, and reproducibility were significant elements for assessing the characteristics of the NIR immunosensor. As displayed in Figure 4C, the selectivity was implemented, carcinoembryonic antigen (CEA), alpha fetoprotein (AFP), prostate specific antigen (PSA), amyloid-β protein (Aβ), glucose (Glu), BSA, procalcitonin (PCT) were applied as the interferences, the ECL intensities of the above interferences (50 ng/mL) were nearly similar to the blank sample. In addition, the ECL response of CYFRA21−1 (1 ng/mL) was almost the same to the mixture (1 ng/mL of CYFRA21−1 and 50 ng/mL of interferences), which displayed a perfect selectivity of the obtained immunosensor. Meanwhile, our immunosensor exhibited excellent operational stability with the relative standard deviation (RSD) of 1.64% (100 fg/mL) and 1.28% (1 ng/mL) for CYFRA21−1 detection under 10 cycles of sustaining sweeping from 0 to +1.2 V (Figure 4D). Neverthless, the positioned stability was also tested by placing the obtained immunosensor for 1−6 days. As exhibited in Figure 4E, the experiment verified that the ECL intensities

https://doi.org/10.1021/acs.analchem.2c01162
Anal. Chem. 2022, 94, 7132−7139

were not disturbed (RSD = 2.62%), which indicated the excellent stability. Then, the reproducibility was investigated by testing 100 fg/mL and 1 ng/mL of CYFRA21−1. As displayed in Figure 4F, there were no distinct differences in the seven electrodes along with low RSD of 2.05% (100 fg/mL) and 1.79% (1 ng/mL), demonstrating the perfect reproducibility of the designed immunosensor.

Analysis of the Real Samples. With the purpose of confirming the clinical application, the constructed immunosensor was used to examine the concentration of CYFRA21−1 and vertify the accuracy through the standard addition method. As displayed in Table 1, the RSD was low than 5% and the recovery ranged from 98 to 101%. In addition, the enzyme-linked immunosorbent assay (ELISA) method was also utilized to test the clinical serum samples. The obtained results were reasonable and displayed good consistence between the two methods as shown in SI Table S2.

Table 1. Recovery Results Obtained from the Prepared ECL Immunosensor

original concentration (ng/mL)	added concentration (ng/mL)	found (ng/mL)	average (ng/mL)	RSD (n = 5, %)	recovery (%)
	1.00	1.79, 1.82, 1.76, 1,77, 1.75	1.78	1.6	98.8
0.800	5.00	5.92, 5.89, 5.96, 5.76, 5.73	5.85	1.7	101
	10.0	10.9, 10.4, 10.7, 10.6, 10.3	10.6	2.2	98.0

CONCLUSIONS

In summary, HDS-$CuCo_2O_4$@Cu_2O heterostructures, an efficient coreactant accelerator developed for promoting the NIR ECL response of Au NCs-TPIA system were first fabricated and utilized in a strongly anticipated immunosensor for CYFRA21−1 detection. Comparing with individual HS-$CuCo_2O_4$ and Cu_2O NPs, the HDS-$CuCo_2O_4$@Cu_2O heterostructures as the electroactive substrate significantly promoted the electrochemical and ECL performance. Furthermore, polypeptide HWR efficiently ameliorated the incubating properties, improving the practical characteristic of the immunosensor greatly. Then, the fabricated immunosensor realized ultrasensitive CYFRA21−1 detection in the range of 2 fg/mL-50 ng/mL with the LOD of 0.67 fg/mL. In the modern bioanalysis, this method could provide new insights of using heterojunctions for accelerating the formation of coreactant intermediate to improve the sensitivity of the immunosensor.

ASSOCIATED CONTENT

Supporting Information

The Supporting Information is available free of charge at https://pubs.acs.org/doi/10.1021/acs.analchem.2c01162.

Chemicals and materials, apparatus; preparation of HDS-$CuCo_2O_4$@Cu_2O-HWR and AuNCs-HWR-Ab_2 bioconjugates; size distribution of AuNCs; high resolution spectra of O 1s; ECL intensity and CV curve for AuNCs without TPIA; the heterostructures of HDS-$CuCo_2O_4$@Cu_2O; EPR spectra; optimization of the experimental conditions; comparison of analytical performances for CYFRA21−1 detection; determination of CYFRA21−1 in clinical serum samples and references (PDF)

AUTHOR INFORMATION

Corresponding Author

Qin Wei − *Collaborative Innovation Center for Green Chemical Manufacturing and Accurate Detection, School of Chemistry and Chemical Engineering, University of Jinan, Jinan 250022, PR China;* orcid.org/0000-0002-3034-8046; Phone: +86 531 82765730; Email: sdjndxwq@163.com; Fax: +86 531 82765969

Authors

Hongying Jia − *Collaborative Innovation Center for Green Chemical Manufacturing and Accurate Detection, School of Chemistry and Chemical Engineering, University of Jinan, Jinan 250022, PR China*

Jingshuai Li − *Collaborative Innovation Center for Green Chemical Manufacturing and Accurate Detection, School of Chemistry and Chemical Engineering, University of Jinan, Jinan 250022, PR China*

Lei Yang − *Collaborative Innovation Center for Green Chemical Manufacturing and Accurate Detection, School of Chemistry and Chemical Engineering, University of Jinan, Jinan 250022, PR China;* orcid.org/0000-0003-2153-3570

Dawei Fan − *Collaborative Innovation Center for Green Chemical Manufacturing and Accurate Detection, School of Chemistry and Chemical Engineering, University of Jinan, Jinan 250022, PR China*

Xuan Kuang − *Collaborative Innovation Center for Green Chemical Manufacturing and Accurate Detection, School of Chemistry and Chemical Engineering, University of Jinan, Jinan 250022, PR China;* orcid.org/0000-0003-0310-6620

Xu Sun − *Collaborative Innovation Center for Green Chemical Manufacturing and Accurate Detection, School of Chemistry and Chemical Engineering, University of Jinan, Jinan 250022, PR China;* orcid.org/0000-0001-8762-4243

Huangxian Ju − *Collaborative Innovation Center for Green Chemical Manufacturing and Accurate Detection, School of Chemistry and Chemical Engineering, University of Jinan, Jinan 250022, PR China;* orcid.org/0000-0002-6741-5302

Complete contact information is available at: https://pubs.acs.org/10.1021/acs.analchem.2c01162

Author Contributions

†H.J. and J.L. contributed equally to this work.

Notes

The authors declare no competing financial interest.

ACKNOWLEDGMENTS

This project was supported by the National Natural Science Foundation of China (21627809 and 21827812), the Special Foundation for Taishan Scholar Professorship of Shandong Province (No. TS201712052) and the Innovation Team Project of Colleges and Universities in Jinan (No. 2019GXRC027).

REFERENCES

(1) Wang, Y. G.; Zhao, G. H.; Chi, H.; Yang, S. H.; Niu, Q. F.; Wu, D.; Cao, W.; Li, T. D.; Ma, H. M.; Wei, Q. *J. Am. Chem. Soc.* **2021**, *143* (1), 504−512.
(2) Yang, L.; Fan, D. W.; Zhang, Y.; Ding, C. F.; Wu, D.; Wei, Q.; Ju, H. X. *Anal. Chem.* **2019**, *91* (11), 7145−7152.
(3) Huang, Y. H.; Zou, R.; Lin, Y. J.; Lu, C. *Anal. Chem.* **2021**, *93* (32), 11291−11297.
(4) Cao, Y.; Zhou, Y.; Lin, Y. H.; Zhu, J. J. *Anal. Chem.* **2021**, *93* (3), 1818−1825.
(5) Zhou, Y.; Chen, S. H.; Luo, X. L.; Chai, Y. Q.; Yuan, R. *Anal. Chem.* **2018**, *90* (16), 10024−10030.
(6) Guo, J. N.; Feng, W. Q.; Du, P. Y.; Zhang, R. Z.; Liu, J.; Liu, Y.; Wang, Z. M.; Lu, X. Q. *Anal. Chem.* **2020**, *92* (21), 14838−14845.
(7) Deng, H. H.; Huan, K. Y.; He, S. B.; Xue, L. P.; Peng, H. P.; Zha, D. J.; Sun, W. M.; Xia, X. H.; Chen, W. *Anal. Chem.* **2020**, *92* (2), 2019−2026.
(8) Huang, Z. N.; Li, Z. L.; Chen, Y.; Xu, L. Y.; Xie, Q. L.; Deng, H. H.; Chen, W.; Peng, H. P. *Anal. Chem.* **2021**, *93* (10), 4635−4640.
(9) Jin, R. C.; Zeng, C. J.; Zhou, M.; Chen, Y. X. *Chem. Rev.* **2016**, *116* (18), 10346−10413.
(10) Jiang, L.; Mi, L.; Wang, K.; Wu, Y. F.; Li, Y.; Liu, A. R.; Zhang, Y. J.; Hu, Z.; Liu, S. Q. *ACS Appl. Mater. Interfaces* **2017**, *9* (37), 31968−31976.
(11) Wang, H. B.; Li, Y.; Bai, H. Y.; Zhang, Z. P.; Li, Y. H.; Liu, Y. M. *Food Anal. Methods* **2018**, *11* (11), 3095−3102.
(12) Zhao, L.; Song, X. Z.; Ren, X.; Fan, D. W.; Wei, Q.; Wu, D. *Anal. Chem.* **2021**, *93* (24), 8613−8621.
(13) Deng, H. H.; Zhang, L. N.; He, S. B.; Liu, A. L.; Li, G. W.; Lin, X. H.; Xia, X. H.; Chen, W. *Biosens. Bioelectron.* **2015**, *65*, 397−403.
(14) Yu, L.; Zhang, Q.; Kang, Q.; Zhang, B.; Shen, D. Z.; Zou, G. Z. *Anal. Chem.* **2020**, *92* (11), 7581−7587.
(15) Miao, W. J.; Choi, J. P.; Bard, A. J. *J. Am. Chem. Soc.* **2002**, *124* (48), 14478−14485.
(16) Wang, T. Y.; Wang, D. C.; Padelford, J. W.; Jiang, J.; Wang, G. L. *J. Am. Chem. Soc.* **2016**, *138* (20), 6380−6383.
(17) Zhu, X. C.; Zhang, X. L.; Zhou, Y.; Chai, Y. Q.; Yuan, R. *Anal. Chem.* **2021**, *93* (29), 10212−10219.
(18) Peng, H. P.; Huang, Z. N.; Deng, H. H.; Wu, W. H.; Huang, K. Y.; Li, Z. L.; Chen, W.; Liu, J. W. *Angew. Chem., Int. Ed.* **2020**, *59* (25), 9982−9985.
(19) Wu, Z. N.; Yao, Q. F.; Chai, O. J. H.; Ding, N.; Xu, W.; Zang, S. Q.; Xie, J. P. *Angew. Chem., Int. Ed.* **2020**, *59* (25), 9934−9939.
(20) Zhou, Y.; Wang, H. J.; Zhuo, Y.; Chai, Y. Q.; Yuan, R. *Anal. Chem.* **2017**, *89* (6), 3732−3738.
(21) Liu, J. L.; Tang, Z. L.; Zhuo, Y.; Chai, Y. Q.; Yuan, R. *Anal. Chem.* **2017**, *89* (17), 9108−9115.
(22) Zhou, Y.; Chai, Y. Q.; Yuan, R. *Anal. Chem.* **2019**, *91* (22), 14618−14623.
(23) Jia, Y.; Yang, L.; Xue, J. W.; Ren, X.; Zhang, N.; Fan, D. W.; Wei, Q.; Ma, H. M. *Biosens. Bioelectron.* **2019**, *144*, 111676.
(24) Jia, Y.; Yang, L.; Xue, J. W.; Zhang, N.; Fan, D. W.; Ma, H. M.; Ren, X.; Hu, L. H.; Wei, Q. *ACS Sens.* **2019**, *4* (7), 1909−1916.
(25) Zheng, J. H.; Liu, X. Y.; Zhang, L. *Chem. Eng. J.* **2020**, *389*, 124339.
(26) Yang, L.; Jia, Y.; Wu, D.; Zhang, Y.; Ju, H. X.; Du, Y.; Ma, H. M.; Wei, Q. *Anal. Chem.* **2019**, *91* (21), 14066−14073.
(27) Lu, N.; Gao, A. R.; Dai, P. F.; Mao, H. J.; Zuo, X. L.; Fan, C. H.; Wang, Y. L.; Li, T. *Anal. Chem.* **2015**, *87* (22), 11203−11208.
(28) Yang, H. O.; Gurgel, P. V.; Williams, D. K., Jr.; Bobay, B. G.; Cavanagh, J.; Muddiman, D. C.; Carbonell, R. G. *J. Mol. Recognit.* **2009**, *23* (3), 271−282.
(29) Valenti, G.; Rampazzo, E.; Kesarkar, S.; Genovese, D.; Fiorani, A.; Zanut, A.; Palomba, F.; Marcaccio, M.; Paolucci, F.; Prodi, L. *Coord. Chem. Rev.* **2018**, *367*, 65−81.
(30) Wu, P.; Hou, X. D.; Xu, J. J.; Chen, H. Y. *Chem. Rev.* **2014**, *114* (21), 11027−11059.
(31) Li, J. F.; Xiong, S. L.; Li, X. W.; Qian, Y. T. *Nanoscale* **2013**, *5* (5), 2045−2054.
(32) Kamari Kaverlavani, S.; Moosavifard, S. E.; Bakouei, A. *Chem. Commun.* **2017**, *53* (6), 1052−1055.
(33) Wang, M. Y.; Sun, L.; Lin, Z. Q.; Cai, J. H.; Xie, K. P.; Lin, C. J. *Energy Environ. Sci.* **2013**, *6* (4), 1211−1220.
(34) An, L.; Huang, L.; Zhou, P. P.; Yin, J.; Liu, H. Y.; Xi, P. X. *Adv. Funct. Mater.* **2015**, *25* (43), 6814−6822.
(35) Zhang, R.; Zhong, X.; Chen, A. Y.; Liu, J. L.; Li, S. K.; Chai, Y. Q.; Zhuo, Y.; Yuan, R. *Anal. Chem.* **2019**, *91* (5), 3681−3686.
(36) Peng, H. P.; Huang, Z. N.; Sheng, Y. L.; Zhang, X. P.; Deng, H. H.; Chen, W.; Liu, J. W. *Angew. Chem., Int. Ed.* **2019**, *58* (34), 11691−11694.
(37) Li, L. L.; Liu, K. P.; Yang, G. H.; Wang, C. M.; Zhang, J. R.; Zhu, J. J. *Adv. Funct. Mater.* **2011**, *21* (5), 869−878.
(38) Wang, H. J.; Yuan, Y. L.; Zhuo, Y.; Chai, Y. Q.; Yuan, R. *Anal. Chem.* **2016**, *88* (4), 2258−2265.

https://doi.org/10.1021/acs.analchem.2c01162
Anal. Chem. 2022, 94, 7132−7139